Supplementary Information for Non-additivity of molecule-surface van der Waals potentials from force measurements

Christian Wagner[1,2], Norman Fournier[1,2], Victor G. Ruiz[3], Chen Li[4], Klaus Müllen[4], Michael Rohlfing[5], Alexandre Tkatchenko[3], Ruslan Temirov[1,2] & F. Stefan Tautz[1,2]

[1]*Peter Grünberg Institut (PGI-3), Forschungszentrum Jülich, 52425 Jülich, Germany*

[2]*Jülich Aachen Research Alliance (JARA)-Fundamentals of Future Information Technology, 52425 Jülich, Germany*

[3]*Fritz-Haber-Institut der Max-Planck-Gesellschaft, Faradayweg 4-6, 14195 Berlin, Germany*

[4]*Max-Planck-Institut für Polymerforschung, Ackermannweg 10, 55128 Mainz, Germany*

[5]*Institut für Festkörpertheorie der Universität Münster, Wilhelm-Klemm-Straße 10, 48149 Münster, Germany*

S1 Sample and tip preparation

The Au(111) single crystal is cleaned using the standard routine of Ar-sputtering and annealing. NTCDA, PTCDA, and TTCDA are deposited at sub-monolayer coverage onto the room-temperature sample by thermal evaporation at $500\,\mathrm{K}$, $570\,\mathrm{K}$, and $710\,\mathrm{K}$, respectively. After deposition, the PTCDA and TTCDA samples are annealed to $470\,\mathrm{K}$ for 2 minutes. Single molecules are created in the STM/nc-AFM by detaching them from the edge of an island with the tip and dragging them several nm away. The tip of the qPlus sensor is made from a PtIr wire of $15\,\mu\mathrm{m}$ diameter that is cut and sharpened by a focused ion beam. The tip apex is covered with gold[1]. This is achieved by carefully dipping it into the Au surface.

S2 Treatment and averaging of experimental raw data

The experimental raw data has been measured in 25 individual contacting experiments (11 on NTCDA, 7 on PTCDA, and 7 on TTCDA). Each of these consists of (1) a vertical approach of the bare Au-covered tip towards the position of one of the carboxylic oxygen atoms within a single isolated surface-adsorbed molecule, (2) the jump to contact at which the carboxylic oxygen atom flips up and forms a covalent bond with the tip, and (3) a series of up to 45 vertical tip retraction and re-approach cycles with the molecule attached to the tip. In all phases the frequency shift of the qPlus sensor is recorded as a function of piezo-voltage (relative z-coordinate z_{rel}).

Irregular curves, which arise as a consequence of either a flip-up of the entire molecule to the tip, a broken tip-molecule bond, or an instability of the tip-suspended molecule are removed

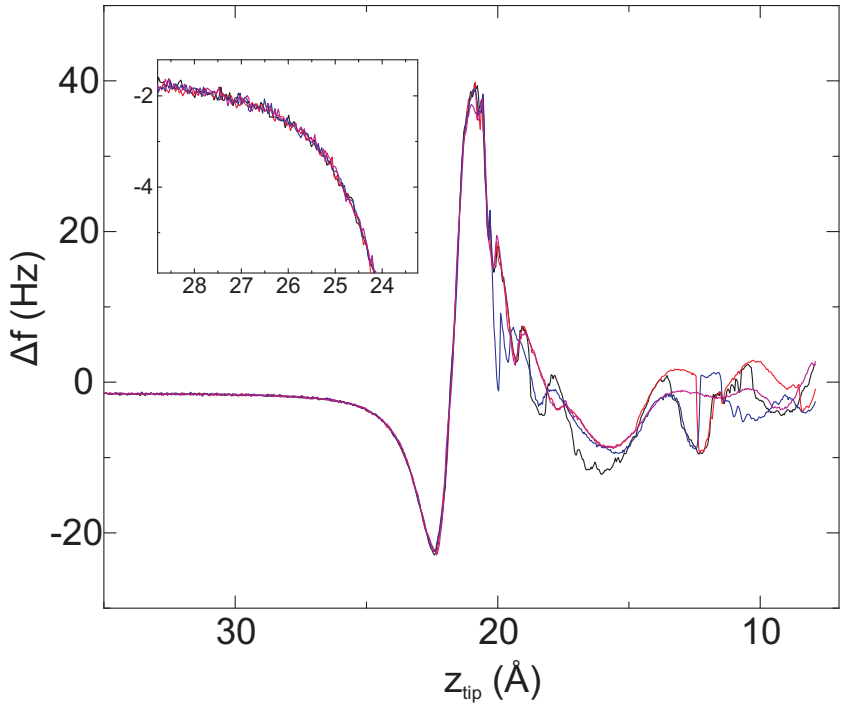

Figure S1: **Exemplary regular raw data curves.** Displayed are four raw data curves taken during two consecutive tip cycles while lifting and lowering TTCDA. The inset shows the noise level and the reproducibility in a relevant region of the curve. The offset of about $1.8\,\mathrm{Hz}$ originates from the tip-sample interaction that is still present in the raw data.

from the data set (about 15% (NTCDA), 20% (PTCDA), and 50% (TTCDA) of all curves). An instability of the suspended molecule is characterized by a pronounced hysteresis between the $\Delta f(z)$ curves taken during retracting and approaching of the tip (Fig. S2). We show exemplary raw data curves in the Figures S1 to S3 to illustrate our criteria for curve-removal.

Within each contacting experiment, the remaining individual $\Delta f(z_{\mathrm{rel}})$ curves are aligned on the z_{rel}-axis with the first re-approach curve, focusing on the part of each curve where the molecule is well separated from the surface. The first re-approach curve is chosen because (1) it is measured

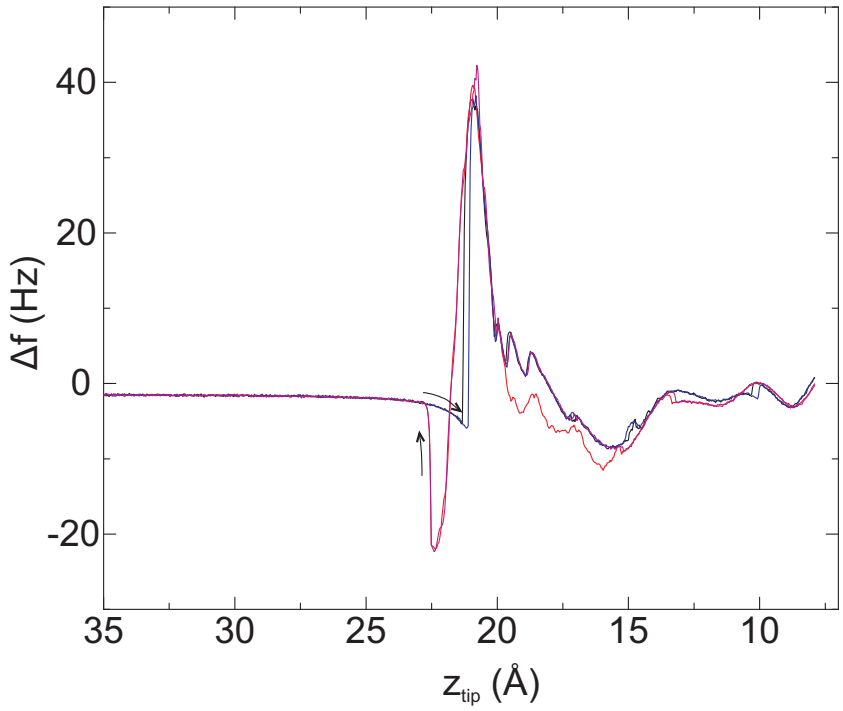

Figure S2: **Exemplary irregular raw data curves.** Displayed are four raw data curves taken during two consecutive tip cycles while lifting and lowering TTCDA. The curves show a clear hysteresis between lifting and lowering of the molecules that originates from instability of the tip-suspended TTCDA molecule or of the tip.

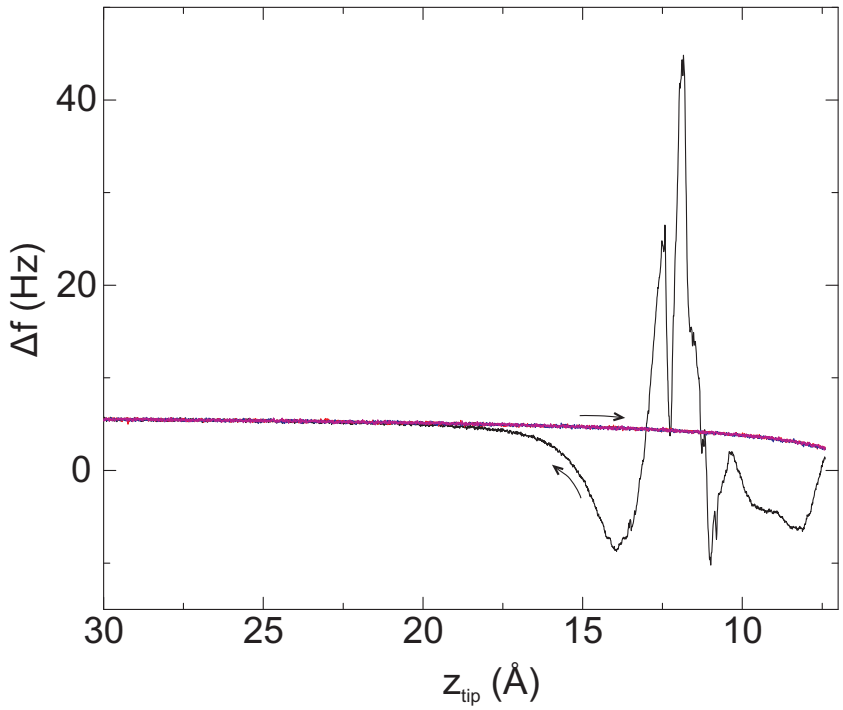

Figure S3: **Exemplary regular and irregular raw data curves.** Displayed are four raw data curves taken during two consecutive tip cycles while lifting and lowering NTCDA. The molecule has flipped to the tip in the last part of the first tip retraction. The subsequently recorded curves show no sign of the molecule in the junction anymore.

in the same direction (tip lowering) as the bare tip approach curve and hence has the same (small) PLL lag, and (2) it is measured shortly after the bare tip approach curve and hence is barely affected by any slow z-piezo creep that may occur. The aligned $\Delta f(z_{\mathrm{rel}})$ curves are averaged. This greatly reduces the noise level.

Next, a fit to the bare tip approach curve $\Delta f_0(z_{\mathrm{rel}})$ is subtracted from the average curve. This step eliminates the tip-surface interaction from the data. Note that the contribution of the single (still flat adsorbed) molecule to the approach curve is too small to be relevant since, at identical tip heights, the tip-suspended vertical molecule is always much closer to the surface than the flat molecule was to the bare tip. This is the reason why the flat molecule's contribution to the bare-tip approach curve can be neglected.

Since the noise level of the bare tip approach curve is that of an individual $\Delta f(z_{\mathrm{rel}})$ curve ($\pm 0.4\,\mathrm{Hz}$) and thus much higher than the noise of the average curve, we subtract a fit to the bare tip approach curve instead of the bare tip approach curve itself. The fit is performed using the 9-parameter function

$$\Delta f_0(z_{\mathrm{rel}}) = -A - C/(B - z_{\mathrm{rel}}) - E/(D - z_{\mathrm{rel}})^2 - G/(F - z_{\mathrm{rel}})^3 - I/(H - z_{\mathrm{rel}})^4 \qquad \text{(S1)}$$

An example of such a fit is shown in Figure S4.

After subtracting the fitted bare tip approach curve, the $\Delta f(z_{\mathrm{rel}})$ curves of individual contacting experiments for one molecular species are aligned on the z_{rel}-axis and averaged again. This further reduces the noise level. Finally, the three resulting curves, one for each molecular species,

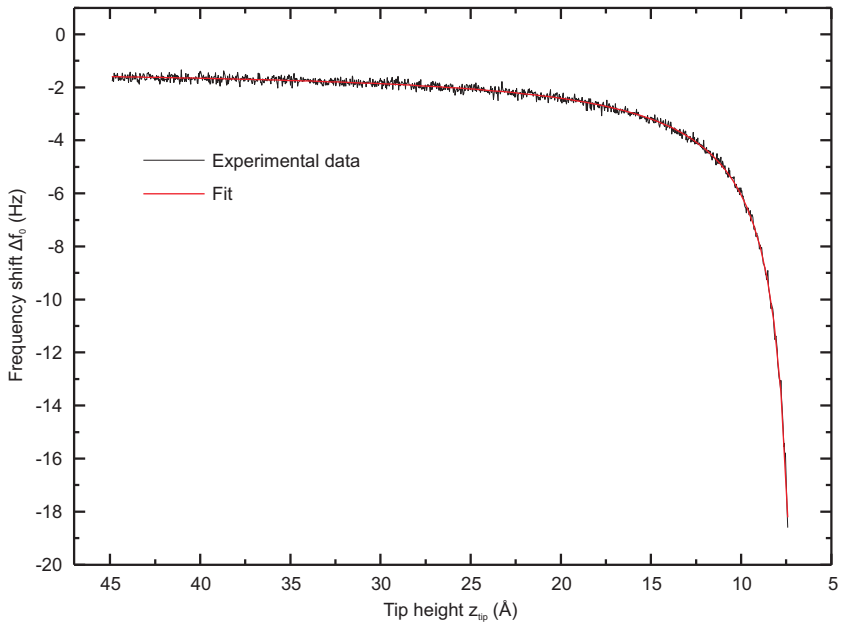

Figure S4: **Exemplary bare tip approach curve and fit.** The fit is subtracted from all Δf curves that have been measured while the molecule is attached to the tip. In this way we completely eliminate the contribution from the tip-surface interaction without introducing additional noise (from the approach curve) in the data.

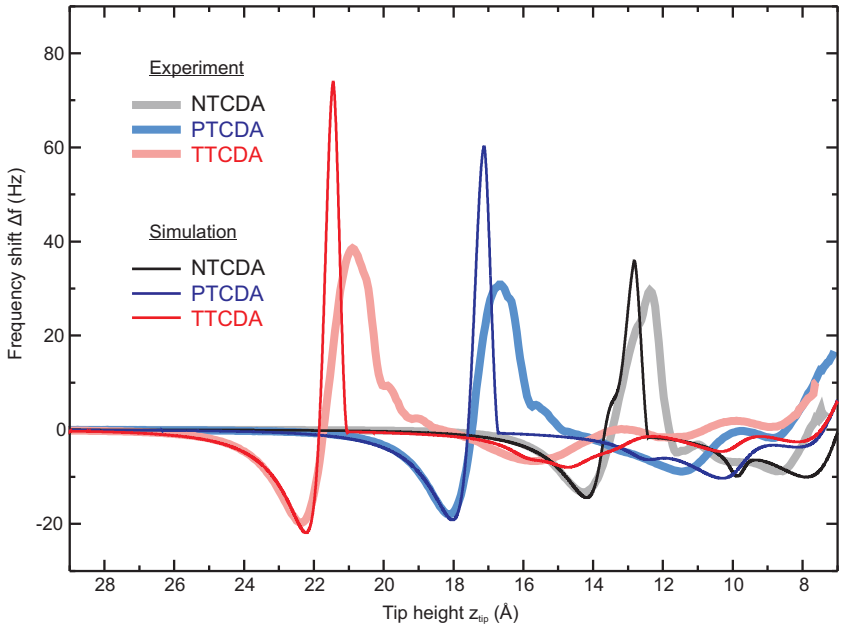

Figure S5: **Determination of the absolute experimental z_{tip}-scale.** Experimental and simulated $\Delta f(z_{\text{tip}})$ curves for the complete single-molecule manipulation process for all three molecules. The experimental data has been aligned to the simulations in the part of the curve where molecule and surface are well separated.

are aligned with respective simulations of the full single-molecule manipulation process that are performed using the procedure and parameters described in Ref. 2 (Fig. S5). This final step provides us with the correctly calibrated z_{tip}-axis. The simulations allow us to employ the known lengths of the molecules as highly accurate rulers for the determination of the absolute tip-sample distance z_{tip} in the experiments.

S3 Multipole expansion for the asymptotic dispersion interaction

A correct description of molecule-surface interaction requires the inclusion of both exchange and correlation at a consistent level. Exchange is the part of the electron-electron interaction energy (beyond the Hartree term) that is related to the anti-symmetric nature of the many-electron wave function[3], while correlation is the correction to the total energy in the Hartree-Fock (HF) approximation[3]. If the distance z between the adsorbate and the substrate is large and there is thus no wave function overlap, there will be no exchange. In this limit, correlation can be treated perturbatively and Lifshitz-Zaremba-Kohn theory (LZK) results in an asymptotic power series $-C_3/z^3 - C_4/z^4 - C_5/z^5 - \ldots$ [4], where C_3 depends on the dipole polarizability of the adsorbate and the bulk macroscopic dielectric function of the metal in the long wavelength $q = 0$ limit (leading order dispersion interaction). Higher order terms include combinations of multipole adsorbate polarizabilities and q-dependent substrate response. In a common approximation we account for the first two terms of this series by

$$V_{\text{a-s}}(z) = -C_3(z - z_0)^{-3}. \tag{S2}$$

The C_3 coefficient in Eq. S2 is given by Ref. 3

$$C_3^{\mathrm{A}_i\mathrm{S}} = \frac{\hbar}{4\pi}\int_0^\infty du \frac{\epsilon_{\mathrm{S}}(iu) - 1}{\epsilon_{\mathrm{S}}(iu) + 1}\alpha_{\mathrm{A}_i}(iu), \tag{S3}$$

with $\epsilon_{\mathrm{S}}(iu)$ being the dielectric function of the metal and $\alpha_{\mathrm{A}_i}(iu)$ the atomic polarizability of species A_i. $z_0 = C_4/3C_3$ gives the position of the van der Waals reference plane that is closely related to the dynamic image plane of the surface[3]. Usually z_0 lies within 20 to 30% of $d_{hkl}/2$, where d_{hkl} is the distance between hkl lattice planes of the hkl substrate surface.

S4 Fit of experimental data

Fit function

The experimental $\Delta f(z_{\text{tip}})$ curves are fitted by the second derivative of Eq. 2 in the paper. The distance d_i of each atom i from the tip at z_{tip} is taken from the simulation results shown in Figure S5. In the region of interest, where molecule and surface are well separated, all atoms in the molecule rigidly move up together with the tip, i.e., the d_i are practically constant over the fitted region.

A clear and direct experimental evidence for a stable molecular configuration of the freely suspended molecule is the lack of any hysteresis between up- and down-cycles (i.e. lifting and lowering of the molecule). If the molecule changed its configuration on the tip during the up-cycle, one would expect the down-cycle to show a different frequency shift curve compared to the up-cycle. Occasionally, this effect was observed (see Fig. S2 and the discussion in Section S2). Those curves were excluded from the data set before averaging and fitting.

Since the dynamic atomic polarizability is element-specific, different C_3 coefficients have to be used for different atomic species in the molecule. This is realized by the combination of element-specific γ_i and a single C_3 which is, by our definition, the C_3 for carbon. We cannot determine the ratios $\gamma_{\text{oxygen}} = C_3^{\text{O-Au}}/C_3^{\text{C-Au}}$ and $\gamma_{\text{hydrogen}} = C_3^{\text{H-Au}}/C_3^{\text{C-Au}}$ from our experimental data, because the fit quality s defined in Eq. S5 depends only very weakly on these ratios. The ratios are therefore taken from our vdW$^{\text{surf}}$ calculation[5], where C_3 coefficients are calculated according to Eq. S3 with $\epsilon_{\text{S}}(iu)$ coming from reflection energy-loss data[6] and $\alpha_{\text{A}_i}(iu)$ from the polarizability of free atoms, scaled by an effective volume for the atom in the molecule that is determined by a

Hirshfeld analysis[7]. The ratios γ_i are used to calculate the effective number of carbon atoms on the abscissa in Fig. 4a as

$$M_{\text{eff}} = \frac{1}{M} \sum_{i=1}^{M} \gamma_i, \tag{S4}$$

where M is the number of atoms in the molecule. We would like to point out that the observation of a non-additivity of the vdW potentials does *not* depend on the partitioning scheme used. For example, if we apply a uniform partitioning scheme with identical C_3 for all atomic species, we obtain $C_3 = 18.7$, $C_3 = 19.7$, and $C_3 = 21.5\,\mathrm{kcal/mol\AA^3}$ for NTCDA, PTCDA, and TTCDA respectively.

Weighted least-squares regression

We use a weighted least-squares regression, minimizing the quantity

$$s = \frac{1}{N} \sum_{j=1}^{N} w_j [\Delta f_{\text{exp}}(z_{\text{tip},j}) - \Delta f_{\text{sim}}(z_{\text{tip},j})]^2 \tag{S5}$$

when fitting the N data points within the fit interval $j = 1, \ldots N$. Choosing the right weights w_j is a non-trivial task.

In the case of a *linear* fit, the goodness of fit (gof) is best described by the reduced χ^2, defined as

$$\chi^2 = \frac{1}{N} \sum_{i=1}^{N} \frac{\left(x_i - x_i^{\text{fit}}\right)^2}{\sigma^2}, \tag{S6}$$

where x_i is the i^{th} measured point and x_i^{fit} the corresponding value of the fitted curve. Here, the respective weighting function is the inverse of the variance σ^2 that is a measure of the statistical noise in the measured curve. While with this definition one obtains $\chi^2 = 1$ for a perfect fit, there is no general rule of how close a reduced χ^2 should be to 1 for a good fit.

For a linear fit the reduced χ^2 as defined above is a suitable gof criterion, because according to this definition each data point of a linear data set has the same chance of contributing to the overall χ^2 value. However, in our case we do not perform a linear fit. Rather, we fit a force law that is proportional to z^{-5} and moreover our experimental noise is practically constant over the whole fit interval. To gauge the quality of our fit to experimental data following this force law, we must ensure that the entire measured curve contributes to our gof criterion. Otherwise, experimental information would be lost, because any part of the measured data curve that does not contribute significantly to the gof criterion has no influence on the outcome of the fit. For this reason we use the gof criterion in Eq. S5 with the weighting function

$$w_j = [|\Delta f_{\text{exp}}(z_{\text{tip},j})| + 0.05\,\text{Hz}]^{-1}. \tag{S7}$$

The normalization by the moduli of the data points ensures that differences $\Delta f_{\text{exp}} - \Delta f_{\text{sim}}$ that are small only because the measured value Δf_{exp} and its fitted value Δf_{sim} are close to zero, will nevertheless contribute to the overall goodness of fit s. The $0.05\,\text{Hz}$ offset prevents singularities that can appear when the signal-to-noise ratio drops below unity and some data points come very close to zero. The value of $0.05\,\text{Hz}$ is derived from the experimental noise level. However, fit results do not change significantly if, for example, $0.1\,\text{Hz}$ is chosen instead.

A comparison of the two gof criteria s and χ^2, displayed in Fig. S6 clearly shows the advantage of our gof criterion s for fitting the z^{-5} power law. In the figure we plot how the gof values s and χ^2 accumulate as we sum over all N data points in the fit interval, starting close to the sample. The reduced χ^2 criterion (blue) puts all the emphasis on the short-distance region (left side), while our gof function s (red) distributes the weight evenly across the whole data range.

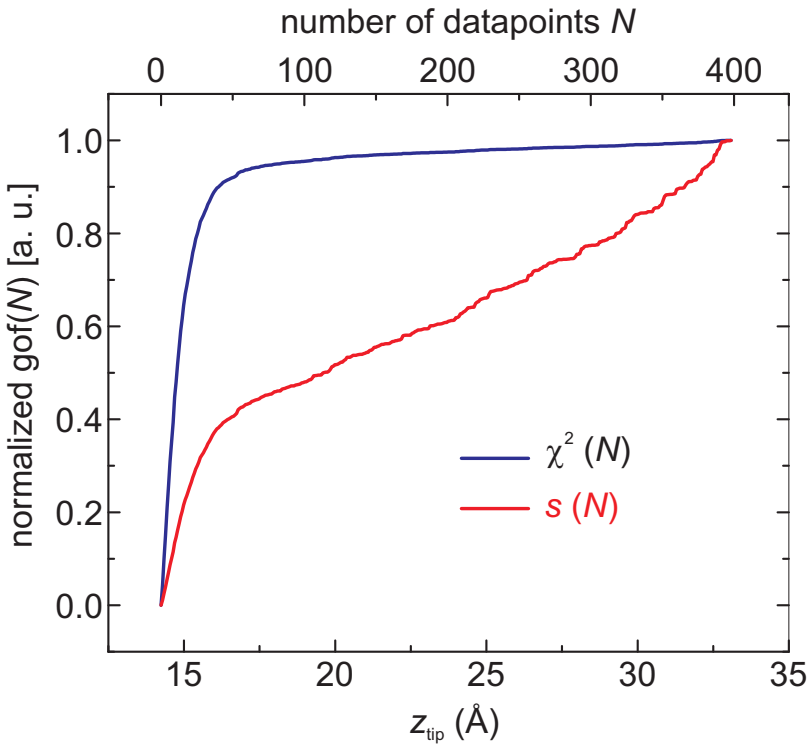

Figure S6: **Comparison of the goodness of fit criteria χ^2 and s.** The exemplary gof values that are shown here have been calculated for a fit to the TTCDA data with a C_3 value which is $1\,\mathrm{kcal/mol\AA^3}$ higher than the optimal fit value. The normalized plots show how χ^2 and s add up to the sum in Eq. S5. The χ^2 criterion reaches 90% of its final value already after the first 10% of the fit interval, while the criterion s takes the full fit interval into account.

The gof values s for our fit are displayed in Fig. 3 in the paper. Having determined the best fit with the gof criterion s, we can also calculate a reduced χ^2 value for our best fit. The respective value is $\chi^2 = 2.3$ (allowing different C_3 for the three molecules). This is to be compared to a reduced χ^2 value of 40 for the best fit that is obtained if the C_3 coefficients of all molecules are constrained to be the same. The residuals of both fits are shown in Fig. 3 of the paper.

Fitting procedure

Because we expect similar reference plane positions z_0 for all three molecules, only one z_0 parameter is necessary for the three experimental $\Delta f(z_{\text{tip}})$ curves. Hence, the data of all three molecules are fitted simultaneously, minimizing a combined s. The parameters to be optimized in the fit are therefore z_0, $C_{3,\text{N}}$, $C_{3,\text{P}}$, $C_{3,\text{T}}$. In addition, a small absolute Δf offset of each of the three experimental $\Delta f(z_{\text{tip}})$ curves is optimized. This offset is in the range of $\pm 0.03\,\text{Hz}$. It accounts for a small remaining uncertainty in our data that is related to the approach curves which have the full $\pm 0.4\,\text{Hz}$ peak-to-peak noise level of a single non-averaged measurement. Although we eliminate this noise completely by using a fit to the approach curve instead of the approach curve itself, the fit is subject to a small uncertainty in said range of $0.03\,\text{Hz}$. To obtain a fully consistent picture, we correct this error by optimizing the respective offset during the fit. The experimental data shown in Fig. 3a have fitted offset values of $0.013\,\text{Hz}$ (NTCDA), $0.02\,\text{Hz}$ (PTCDA), and $0.0\,\text{Hz}$ (TTCDA). As we do not presuppose a theoretical value for z_0, but obtain it from the fit, any error in the molecule-surface distance determination would just result in a wrong value for z_0, but not for the C_3 coefficients (cf. Eq. 1-3 in the paper). The fact that we obtain a value for z_0 that is very close to theoretical expectations proves in turn that our initial distance determination is accurate within

a small fraction of an Angstrom.

Since there may be local minima in the fit quality s as a function of the 7 fit parameters, we use a robust fitting method that searches the whole parameter space around the expected minimum for z_0 and the Δf offset values, while using a method with decreasing step size for the optimization of the individual C_3 coefficients.

Experimental error via synthetic noise

An unavoidable source of error in the recovered C_3 coefficients is the statistical noise in the experimental Δf curves. It is not a priori clear how strongly the noise of about $0.02\,\mathrm{Hz}$ (NTCDA and TTCDA) and $0.05\,\mathrm{Hz}$ (PTCDA) affects our fitting procedure and thus the recovered C_3 values. To estimate the error, we use a Monte Carlo approach, adding white noise of the respective amplitude to the data in Fig. 3a and conducting the fit. From the statistical distribution of the C_3 values recovered in 140 such runs we obtain an estimate of the statistical error. The resulting error bars are shown in Fig. 4a.

S5 Discussion and exclusion of potential systematic errors

qPlus sensor stiffness

The stiffness of commercially available qPlus sensors is $1800 \pm 100\,\mathrm{N/m}$. This uncertainty introduces a systematic error in the determined C_3 coefficients of about 6%, which does, however, not influence the observed superlinearity.

Electrostatic forces

In principle, electrostatic forces between the tip (with the attached molecule) and the surface could add to the experimentally measured frequency shifts and thus invalidate the fitting of our data that is based on van der Waals forces only. Electrostatic forces could originate from contact potential differences between the tip with attached molecule and the surface. Such contact potential differences could arise from charge transfer between the tip and the molecule. In particular, if there was a systematic variation in this charge transfer with the molecules in our homologuous series, electrostatic forces could influence the observed superlinearity of the C_3 coefficients. It is important to realize that we only need to consider electrostatic effects that are related to the tip-attached molecule, since *all* (bare) tip-surface interactions (van der Waals *and* electrostatic) are eliminated from the measured data by subtraction of the bare tip approach curve (see Section S2).

To address this issue, we have carried out DFT calculations of the tip-molecule-surface junction, with and without van der Waals interactions (PBE and PBE + $\mathbf{vdW}^{\mathrm{surf}}$). DFT calculations determine the charge distribution in the junction, including possible charge rearrangements between the tip (modeled by a 20 atom pyramidal cluster) and the molecule, and on this basis yield the electrostatic interaction energy (electrostatic forces) between the molecule-decorated tip and the surface. We note here that the DFT calculations are very expensive, because the system-size is large and the sought-after interaction energies are very small, on the border of what is feasible.

Our DFT calculations show that there is no systematic change of the charge transfer between tip and molecule in the homologous series NTCDA-PTCDA-TTCDA, and hence no systematic

change of the contact potential that could explain the superlinearity of our C_3 coefficients. In fact, the (molecule related; see above) electrostatic interaction energies between the molecule-decorated tips and the surface are exceedingly small (at $z_{\mathrm{mol}} = 7\,\text{Å}$ $-3.1\,\mathrm{meV}$ for NTCDA, $-5.1\,\mathrm{meV}$ for PTCDA and $-2.1\,\mathrm{meV}$ for TTCDA) and, most importantly, do not increase in the sequence from NTCDA to TTCDA, as would be necessary if systematic contact potential differences were to be invoked to explain the superlinearity of the experimentally determined C_3 coefficients. Moreover, even at the relatively close distance of $z_{\mathrm{mol}} = 7\,\text{Å}$, the DFT+vdW$^{\mathrm{surf}}$ calculated van der Waals interaction energies are approximately one order of magnitude larger (26.6 to 33.5 meV) than the electrostatic energies. Furthermore, there is strong experimental evidence (confirmed by DFT calculations) that also for PTCDA on a flat Au(111) surface there is essentially no charge transfer to the molecule[8]. Since no charge transfer is present in either of the two extreme cases (sharp Au tip and flat Au(111) surface), we can conclude that charge transfer for our real experimental tip is also negligible.

On the basis of the detailed DFT study, we can thus conclude that electrostatic interaction does not play a significant role in the present material system xTCDA/Au(111). This is in full agreement with our experimental findings and the interpretation of our data.

Orientation of the molecule

In our fitting of equation (2) to the experimental data we employ a vertical orientation of the molecule (i.e. the diagonal of the molecule is perpendicular to the surface). This orientation is obtained by minimizing the molecule-surface vdW potential for the tip-suspended molecule. If

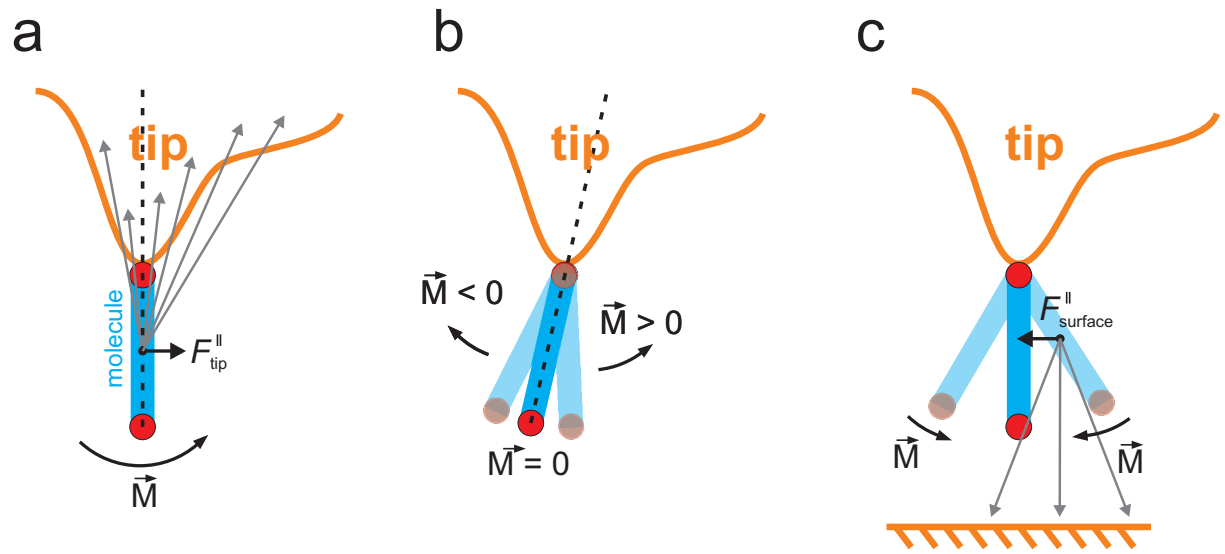

Figure S7: **Sketch of the forces and resulting torques acting on the molecule. a** Asymmetries in the mesoscopic tip apex can lead to lateral forces acting on the tip-suspended molecule. **b** If the bond between molecule and tip apex has no directionality (as in the present case), and if the molecule experiences attractive forces to the tip only, the molecule will always end up sitting flat on the tip, because the equilibrium of a molecule not sitting flat on the tip will always be unstable. **c** The molecule-surface attraction introduces a restoring force strictly towards the vertical molecular orientation.

there was in experiment a deviation from this orientation, this would have an influence on the determined C_3 coefficients (this is, in fact, obvious from equation 2). However, we demonstrate below by means of an ab-initio DFT calculation and experimental evidence that obtaining the molecular orientation by minimizing the molecule-surface vdW potential (and thus the vertical orientation as defined above) is indeed justified.

In our DFT calculation (PBE functional) we start with a molecule that is suspended vertically

off the tip and tilt this molecule in the molecular plane and perpendicular to it. The incurred energy cost is of the order of $10\,\mathrm{meV}$ in an angle range of $\pm 20^\circ$ (the tilting perpendicular to the molecular plane incurs an even smaller energy cost of $< 2\,\mathrm{meV}$). Since these numbers are at the significance threshold of DFT, the calculation confirms that for our molecules the gold-oxygen bond has essentially no directionality. The orientation of the molecule hanging off the tip will therefore be determined by van der Waals forces alone (electrostatic forces are negligible, as discussed above). There are two sets of van der Waals forces of relevance here: (1) F_{surface} between the molecule and the surface and (2) F_{tip} between the molecule and the tip. For symmetry reasons, F_{surface} is always directed strictly normal to the surface, while F_{tip} can (and most probably will) deviate from this direction, depending on asymmetries of the tip shape (see Figure S7a). $F_{\text{tip}}^{||}$, the parallel component of F_{tip}, is related to the imbalance between the attractions to opposite sides of the tip and produces a torque M on the molecule, as indicated in Figure S7a.

If for the moment we disregard F_{surface}, we see in Figure S7b that on an asymmetric tip the molecule will assume an equilibrium position ($M = 0$) that is tilted away from the more massive side of the tip. In this way the presence of more tip matter on the right hand side is balanced by the closer vicinity of the molecule to the left hand side of the tip (Figure S7b). What is also immediately obvious from Figure S7b is the fact that the equilibrium of a molecule that experiences only attractive forces to the tip is always unstable: Any tilt to one side will produce a torque that will turn the molecule further to that same side, until the molecule sits flat on the tip. This is shown schematically by the curve marked with E_{tip} in Figure S8, where the potential energy E is plotted against the tilt angle θ. We can thus conclude: If the bond between molecule and tip apex

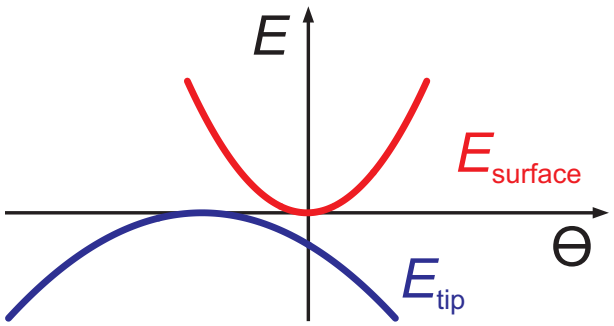

Figure S8: **Schematic angle dependent potential**

has no directionality (as in the present case), and if the molecule experiences attractive forces to the tip only, the molecule will always end up sitting flat on the tip. Evidently, such a molecule is undetectable in our experiments (see Fig. S3).

The facts that (i) in many cases we still detect the molecule in the junction when we return the tip towards the surface from far away, and that (ii) the corresponding frequency shift curves fall on top of the Δf curves measured on retraction of the tip with the hanging molecule from the surface (i.e. no hysteresis), thus mean that there must be additional forces acting on the molecule which turn the unstable equilibrium of the hanging molecule into a stable one, such that no flip to the tip can occur. These forces can only originate from the surface (since the tip-molecule bond is not directional, see above). Indeed, Figure S7c shows that van der Waals attraction to the surface generates torques that turn the molecule towards the vertical orientation. The corresponding potential energy curve is also shown in Figure S8, labelled E_{surface}. The total potential energy is given by the sum of the two curves (not drawn).

Now Figure S8 shows very clearly: In order for the molecule to survive the whole manipula-

tion cycle in the hanging configuration (with maximum tip-surface distances of 45 Å at the upper turning point), the total potential energy curve must be opening upwards throughout the complete cycle (otherwise the molecule would flip to the tip). Therefore the potential curve E_{tip} must always be shallower than E_{surface} in this cycle. Since the van der Waals attraction to the surface at the upper turning point of the manipulation cycle is very weak and therefore E_{surface} is very shallow, the potential energy curve E_{tip} must be even shallower. Note that E_{tip} itself does not depend on the tip-surface distance. In other words, the restoring force constant $k^{||}_{\text{surface}}$ due to the minimal van der Waals attraction to the surface constitute an upper bound for the parallel force constant $k^{||}_{\text{tip}}$ due to the tip throughout the complete manipulation cycle (i.e. $k^{||}_{\text{surface}} > k^{||}_{\text{tip}}$ always, with $k^{||}_{\text{surface}} >> k^{||}_{\text{tip}}$ for most of the manipulation cycle since $F_{\text{surface}} \propto z^{-4}_{\text{mol}}$ increases rapidly with decreasing z_{mol}).

In conclusion, this means that in all those manipulation cycles in which the molecule survives in the hanging configuration, the molecule must reside very close to the vertical configuration for most of the fitting range, because in most the fitting range $k^{||}_{\text{surface}} >> k^{||}_{\text{tip}}$. We note here that the improvement of the fit due to allowing for superlinearity is achieved in a distance range quite close to the sample (see Fig. 3a of the manuscript) where the surface-derived torque on the molecule is strong, leading to a vertical orientation. Hence, we can positively exclude that our finding of superlinearity is influenced in any way by a deviation of the molecular orientation from the vertical.

According to Figs. S7a and S7b, a tip with a small $k^{||}_{\text{tip}}$ is a nearly symmetric tip. One may ask why we have succeeded in preparing a relatively large number of symmetric tips. The answer

is clear: Only symmetric tips allow complete, non-hysteretic manipulation cycles. By eliminating hysteric curves form our data set, we automatically eliminate asymmetric tips which would lead to significantly tilted molecules. This means in summary: While it is true that tilts of the molecule will influence the obtained C_3 values, we can exclude such tilts on experimental grounds and thus obtain C_3 coefficients that are not influenced by tilts.

S6 The DFT+vdW$^{\mathrm{surf}}$ methodology

The DFT+vdW$^{\mathrm{surf}}$ method consists in the combination of the DFT+vdW method[9] for treating intermolecular interactions in density-functional theory (DFT) and the Lifshitz-Zaremba-Kohn (LZK) theory[4,10] for the nonlocal many-body response of the substrate surface. The inclusion of these collective many-body effects, present within the substrate, in the determination of the vdW interaction effectively goes beyond an atom-based pairwise description.

Based on the LZK theory, the interaction coefficient $C_3^{\mathrm{A}_m\mathrm{S}}$ between atomic species A_m and substrate S is given by

$$C_3^{\mathrm{A_mS}} \;=\; \frac{\hbar}{4\pi}\int_0^\infty d\omega \frac{\varepsilon_{\mathrm{S}}(i\omega)-1}{\varepsilon_{\mathrm{S}}(i\omega)+1}\,\alpha_{\mathrm{A}_m}(i\omega), \tag{S8}$$

where $\epsilon_{\mathrm{S}}(i\omega)$ is the dielectric function of solid S (Au in the present case) calculated from reflection energy–loss spectroscopy experiments[6] and $\alpha_{\mathrm{A}_m}(i\omega)$ corresponds to the dipole polarizability of atomic species A in molecule m, where $m = \{\mathrm{N},\mathrm{P},\mathrm{T}\}$ as defined in the main text for [N]TCDA, [P]TCDA, and [T]TCDA. For the element-specific dipole polarizabilities $\alpha_{\mathrm{A}_m}(i\omega)$, we rely on a Padé approximant model[9,11] as in the DFT+vdW method, given by the leading term of the Padé

series as:

$$\alpha_{\mathrm{A}_m}(i\omega) \;=\; \frac{\alpha^0_{\mathrm{A}_m}[n(\mathbf{r})]}{1+(\omega/\eta_{\mathrm{eff}})}, \tag{S9}$$

where η_{eff} is an effective characteristic excitation frequency and $\alpha^0_{\mathrm{A}_m}(i\omega)$ corresponds to an element-specific isotropic static dipole polarizability. The latter is a functional of the ground-state electron density $n(\mathbf{r})$ of the atom in the molecule given as $\alpha^0_{\mathrm{A}_m}[n(\mathbf{r})] \;=\; v_{\mathrm{eff}}^{\mathrm{A}_m}[n(\mathbf{r})]\alpha^0_{\mathrm{A}_{\mathrm{free}}}$, where $\alpha^0_{\mathrm{A}_{\mathrm{free}}}$ corresponds to the static dipole polarizability of the free atom obtained from high level quantum chemical calculations, and $v_{\mathrm{eff}}^{\mathrm{A}_m}[n(\mathbf{r})]$ is the definition of a dimensionless effective volume for species A_m referenced to the free atom in terms of the Hirshfeld partitioning of the electron density (see Refs. 5, 7, 9, 12).

In order to compute the effective volumes $v_{\mathrm{eff}}^{\mathrm{A}_m}$ for each species A in molecule m, we performed DFT calculations for the case of a single [N,P,T]TCDA molecule on a Au(111) surface using the PBE exchange-correlation functional[13]. The effective volumes are given by

$$v_{\mathrm{eff}}^{\mathrm{A}_m} = \left(\frac{\int r^3 w_{\mathrm{A}}(\mathbf{r}) n^m(\mathbf{r}) d^3\mathbf{r}}{\int r^3 n_{\mathrm{A}}^{\mathrm{free}}(\mathbf{r}) d^3\mathbf{r}}\right), \tag{S10}$$

where $w_{\mathrm{A}}(\mathbf{r})$ is the Hirshfeld atomic partitioning weight of the species A, r^3 is the cube of the distance from the nucleus of an atom A, $n^m(\mathbf{r})$ is the total electron density of molecule m, and $n_{\mathrm{A}}^{\mathrm{free}}(\mathbf{r})$ is the reference electron density corresponding to the free atom A.

All calculations were performed with the FHI-AIMS code[14]. The repeated-slab method was used to model all three systems, with three metallic layers to perform the calculations in-line with previous investigations[5,8,15–17]. We used the experimental lattice constant of Au (4.065 Å) to build the (111) surface and a Monkhorst-Pack[18] grid of $2 \times 2 \times 1$ k-points in the reciprocal space. For

Table S1: Interaction coefficients C_3 given in $\left(\frac{\mathrm{kcal}}{\mathrm{mol}}\mathrm{\AA}^3\right)$ for Au with each atomic species in the molecule and the weighting factors γ_{A} (dimensionless) are presented. The interaction coefficients of Au with each species A as a free atom are included for reference. By definition, γ_{C} is equal to 1.00.

	$C_3^{\mathrm{C}_m\mathrm{Au}}$	$C_3^{\mathrm{H}_m\mathrm{Au}}$	$C_3^{\mathrm{O}_m\mathrm{Au}}$	γ_{H}	γ_{O}	γ_{C}
NTCDA	27.0	7.7	18.0			
PTCDA	27.3	7.9	18.4	0.29	0.67	1.00
TTCDA	27.3	8.0	18.3			
Free atom	32.6	12.2	19.4	0.37	0.60	1.00

each system, the volumes $v_{\mathrm{eff}}^{\mathrm{A}_m}$ were calculated with the molecule placed at distances larger than 4.0 Å with respect to the topmost unrelaxed substrate layer. The final values taken for the calculation of $\alpha^0_{\mathrm{A}_m}(i\omega)$ correspond to the distance averaged value in each system.

Using the theory described above, we computed the interaction coefficient $C_3^{\mathrm{A}_m\mathrm{Au}}$ for C, H, and O in the [N,P,T]TCDA molecules with Au(111) as substrate. We define the weighting factor γ_{A} for species A with respect to Carbon as $\gamma_{\mathrm{A}} = \frac{1}{3}\sum_m^3 \gamma_{\mathrm{A}_m}$, where $\gamma_{\mathrm{A}_m} = C_3^{\mathrm{A}_m\mathrm{Au}}/C_3^{\mathrm{C}_m\mathrm{Au}}$ and $m = \{\mathrm{N}, \mathrm{P}, \mathrm{T}\}$ as described in the text above. The results are given in Table S1.

S7 Deviations from the asymptotic dispersion interaction at short range

We found in the paper that below ≈ 4.8 Å the asymptotic form Eq. S2 of the dispersion interaction is not fulfilled any more (Fig. 3b). This is to be expected, because Eqs. S2 and S3 only constitute the long-range limit of the more general expression for the interaction part ($V_{\mathrm{a-s}}$) of the entire correlation energy E_{C} (see Section S3 of the Supplementary Information). In the random phase approximation (RPA) to the adiabatic-connection fluctuation-dissipation theorem (ACFDT)[17,19–21] the correlation energy E_{C} is given by

$$E_{\mathrm{C}} = -\frac{1}{2\pi}\int_0^\infty du \mathrm{Tr}\left(\underline{\underline{1}} - \underline{\underline{\epsilon}}(iu) + \ln(\underline{\underline{\epsilon}}(iu))\right) \tag{S11}$$

with $\underline{\underline{\epsilon}}(\omega)$ being the space-dependent dielectric function (or, equivalently, its Fourier-transform matrix as discussed below in Section S8 of the Supplementary Information) of the entire system of surface plus atom/molecule.

The RPA total energy, being an approximation, might suffer from slight inaccuracies on an absolute energy scale. Nonetheless, RPA is perfectly suitable as a basis on which the deviation of van der Waals attraction from its long-range asymptotic behaviour at close distances can be discussed.

At large distances the charge densities of substrate and atom/molecule do not overlap, and $\underline{\underline{\epsilon}}(\omega)$ can be simplified into individual contributions from surface and atom/adsorbate, finally leading to the expressions of Eqs. S2 and S3. At closer distances, however, the charge densities and polarizabilities of surface and of atom/molecule overlap and influence each other in a way which

prohibits separation. The evaluation of Eq. S11 for physisorption of PTCDA on Ag(111) shows that $V_{\mathrm{a-s}}(z)$ becomes weaker than Eq. S2 for z smaller than about 4-5 Å [17], and does not diverge at z_0. This makes the use of Eq. S2 questionable at typical physisorption distances, as is indeed found in our fits if the fitting region starts at too low values of z_{mol}.

S8 C_3 coefficients from the random phase approximation

Fig. 4a contains C_3 coefficients based on the random phase approximation (RPA) to the adiabatic-connection fluctuation-dissipation theorem (ACFDT)[17,19–21]. The calculation is based on Eq. S3 with RPA-calculated molecular polarizabilities and ϵ_{S} for the metal from Ref. 22.

Since we are in the limit of clearly separated subsystems surface and molecule, we have to use the *macroscopic* dipole polarizability α_{macr} which is defined as the dipole response to the *macroscopic* electric field. But we need to calculate the macroscopic response of the molecule from a full *microscopic* quantum theory of the molecule, because we are interested in the role played by the quantum mechanical electronic states in the response.

The evaluation of the α in Eq. S3 starts with the microscopic density-density response function

$$\chi(\mathbf{r},\mathbf{r}',\omega) = -4\frac{1}{V}\sum_{m}^{occ}\sum_{n}^{empty}\psi_m(\mathbf{r})\psi_m^*(\mathbf{r}')\psi_n^*(\mathbf{r})\psi_n(\mathbf{r}')\frac{E_n - E_m}{(E_n - E_m)^2 - \omega^2} \tag{S12}$$

at the RPA level. This function reveals how a perturbation of the density at position $\mathbf{r}$ within the molecule propagates to position $\mathbf{r}'$. The $|m\rangle$, $|n\rangle$ are the quantum mechanical states of the electrons in the molecule. From Eq. S12, we calculate the Fourier transform $(\underline{\underline{\chi}}(\omega))_{\mathbf{Q},\mathbf{Q}'}$, where

in our notation the matrix $(\underline{\underline{f}})_{\mathbf{Q},\mathbf{Q}'}$ is the Fourier transform of $f(\mathbf{r},\mathbf{r}')$. $(\underline{\underline{\chi}}(\omega))_{\mathbf{Q},\mathbf{Q}'}$ is related to the microscopic dielectric function $(\underline{\underline{\epsilon}}(\omega))_{\mathbf{Q},\mathbf{Q}'}$ by a matrix-matrix multiplication with the bare Coulomb interaction $(\underline{\underline{v}}(\omega))_{\mathbf{Q},\mathbf{Q}'}$

$$(\underline{\underline{\epsilon}}(\omega))_{\mathbf{Q},\mathbf{Q}'} = 1 - (\underline{\underline{v}})_{\mathbf{Q},\mathbf{Q}'}(\underline{\underline{\chi}}(\omega))_{\mathbf{Q},\mathbf{Q}'} \tag{S13}$$

In Fourier space, we can obtain the inverse microscopic dielectric function $(\underline{\underline{\epsilon}}^{-1}(\omega))_{\mathbf{Q},\mathbf{Q}'}$ by a simple matrix inversion. The *macroscopic* dielectric constant is defined as the long-range limit of the inverse dielectric function, which can be obtained in Fourier space as

$$\epsilon^{-1}_{\mathrm{macr}}(\omega) = (\underline{\underline{\epsilon}}^{-1}(\omega))_{\mathbf{Q}=0,\mathbf{Q}'=0}. \tag{S14}$$

Finally, we have to relate the macroscopic dielectric function to the macroscopic polarizability that can be used in Eq. S3. Here we use the fact that the polarization density $\mathbf{P} = \mathbf{p}/\mathbf{V}$, where V is the volume, can be expressed by

$$\mathbf{P}(\mathbf{r}) = \frac{\epsilon_{\mathrm{macr}} - \mathbf{1}}{\mathbf{4\pi}}\mathbf{E}(\mathbf{r}), \tag{S15}$$

where $\mathbf{E}(\mathbf{r})$ is the macroscopic electric field. Combining this with the definition of the macroscopic polarizability $\mathbf{p}(\mathbf{r}) = \alpha_{\mathrm{macr}}\mathbf{E}(\mathbf{r})$ we obtain

$$\alpha_{\mathrm{macr}}(\omega) = \frac{V}{4\pi}(\epsilon_{\mathrm{macr}}(\omega) - 1). \tag{S16}$$

$\alpha_{\mathrm{macr}}(\omega)$ at imaginary frequencies is then inserted into Eq. S3. We note that for anisotropic objects like the molecules under consideration here, different directions along which the $\mathbf{Q}, \mathbf{Q}'$ approach zero in Eq. S14 lead to different dielectric functions. In other words, $\epsilon_{\mathrm{macr}}(\omega)$ and $\alpha_{\mathrm{macr}}(\omega)$ are 3×3 tensors. Because of the symmetry of our molecules, these tensors become diagonal if the

coordinate system is chosen to coincide with the three symmetry directions (principal axes), such that the macroscopic polarizability is fully described by the three functions $\alpha_{xx}(\omega)$, $\alpha_{yy}(\omega)$ and $\alpha_{zz}(\omega)$. Note that we use a molecular coordinate system in which x refers to the long molecular axis within the plane of the molecule, y refers to the short axis, and z is perpendicular to the molecular plane.

S9 Superlinearity

In the paper we found a clear trend of increasing experimental C_3 coefficients with molecular size, i.e. the per-atom molecule-surface interaction rises in the sequence NTCDA $\rightarrow$ PTCDA $\rightarrow$ TTCDA. Slight inaccuracies of the RPA total energy on an absolute energy scale notwithstanding, the RPA (see Sections S7 and S8 of the Supplementary Information) is perfectly suitable as a basis to discuss the connection between the microscopic electronic states and the macroscopic polarizability of the molecule that finally leads to the superlinear increase of the C_3 coefficients.

Eqs. S12 to S16 indicate two important issues regarding the macroscopic polarizability α_{macr} and its separation into contributions from individual atoms. On the one hand, the microscopic charge-density response χ in Eq. S12 can often be discussed in terms of local, atom-wise polarizability effects (simply because the various wave functions have local contributions at the various atoms). However, after the transformation $\chi \rightarrow \epsilon \rightarrow \epsilon^{-1} \rightarrow \epsilon^{-1}_{\mathrm{macr}} \rightarrow \alpha_{\mathrm{macr}}$, which shuffles information around in real space (in terms of the so-called local-field effects), atom-wise additivity is questionable. This is in principal contrast to the idea of the additivity of atom-to-atom contribu-

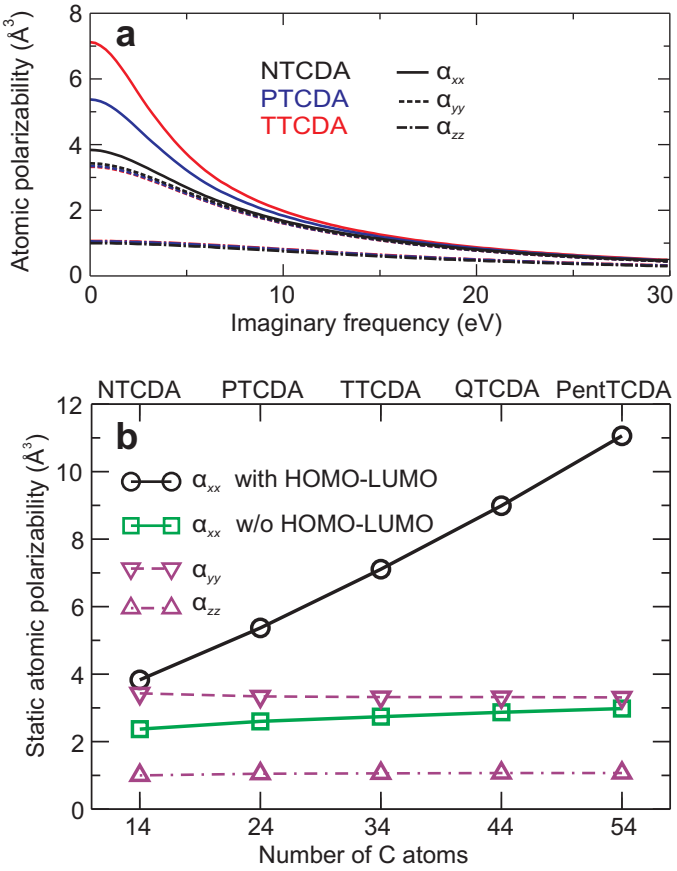

Figure S9: **a** Dynamic per-atom polarizabilities of carbon (averaged over all atoms in the molecule) for NTCDA, PTCDA, and TTCDA as resulting from Eq. S12. Local-field effects are not included here, so the polarizabilities are larger than those observable in experiment. The coordinates x, y, and z refer to the directions along the long axis, short axis, and perpendicular to the plane of each molecule. **b** Static per-atom polarizabilities of carbon (averaged over all atoms in the molecule) for NTCDA, PTCDA, TTCDA, QTCDA, and PentTCDA (same as the zero-frequency data of panel a). The data labelled "w/o HOMO-LUMO" are obtained by excluding the HOMO-LUMO transition from the summation of Eq. S12.

tions to the van der Waals interaction. Fortunately, such effects are often of secondary importance. In the present case of NTCDA, PTCDA, TTCDA and beyond, our calculations indicate that the molecular polarizabilities before and after the $\chi \rightarrow \epsilon \rightarrow \epsilon^{-1} \rightarrow \epsilon^{-1}_{\rm macr} \rightarrow \alpha_{\rm macr}$ transformation differ by a factor that is the same for all molecules discussed here. This would re-establish the additivity, if it were not for the second issue to which we now turn.

Eq. S12 indicates that even at the level of the microscopic density response function χ, the polarizability of an atom is drastically influenced by its environment, because the latter affects the wave functions and the energy levels. This influence can be quite long-ranged if delocalized quantum mechanical states dominate the polarizability. We discuss this issue in more detail below for the case of NTCDA, PTCDA, and TTCDA. In short, the delocalized nature of quantum mechanical states makes it impossible to accurately predict the polarizability of an atom from just considering its nearest neighbours.

As an example, we show in Figure S9a the per-atom polarizability of the carbon atoms (averaged over all carbon atoms in each molecule) for NTCDA, PTCDA, and TTCDA for imaginary frequencies iu that are relevant for Eqs. S3 and S11. The data result from Eq. S12 by partitioning the wave functions into contributions at each atom (for details, see Ref. 23). We also evaluate the anisotropy of the charge-density response of Eq. S12, which is particularly important for the current case of flat π-conjugated systems. Note that all discussion here are on the level of χ (more precisely $(\underline{\underline{\chi}}(\omega))_{\mathbf{Q}=\mathbf{0},\mathbf{Q}'=\mathbf{0}}$), i.e. Eq. S12, without considering local-field effects.

Three important observations can be made in Figure S9a:

- At large iu, the per-atom polarizability behaves as $\chi \propto u^{-2}$. This is expected from Eq. S12 if $u \gg E_n - E_m$. Moreover, at large iu the per-atom polarizability is essentially the same for all molecules.

- There is a strong anisotropy of the per-atom polarizability. This is coupled to the linear extensions of the molecule in the three space directions. The larger the extension in a given direction, the larger the respective polarizability. Note that NTCDA, which is of similar extension in x and y directions, also has similar per-atom polarizabilities in these two directions.

- As $iu \to 0$, we observe a strong difference in χ_{xx} between NTCDA, PTCDA, and TTCDA. Looking at Eq. S12, we would expect such a behaviour if $E_n - E_m$ was decreasing in the same sequence. Since the HOMO-LUMO transition is by definition the lowest energy transition in each molecule that therefore contributes strongest to the atomic polarizability $\chi \propto (E_n - E_m)^{-1}$ in Eq. S12, this suggests that the HOMO-LUMO gap drops in the sequence NTCDA $\to$ PTCDA $\to$ TTCDA. This is indeed true. It is remarkable that χ_{yy} and χ_{zz} are apparently not affected by the changing HOMO-LUMO gap, with the consequence that the per-atom polarizabilities along y and z are nearly the same for all molecules. This is also found for all per atom polarizabilities of the oxygen and hydrogen atoms.

The strong increase of the per-atom polarizability along x (the long axis of the molecule) for increasing length of the molecule (NTCDA$\to$PTCDA$\to$TTCDA) is the origin of the superlinearity of the C_3 coefficients as discussed in the paper.

A more detailed analysis confirms the role of the HOMO-LUMO transition as conjectured above. In Figure S9b the same data as in panel **a** is displayed, but for zero frequency only (static case). For the data labelled "w/o HOMO-LUMO" the HOMO-LUMO transition has been left out of the summation in Eq. S12. Evidently, the per-atom polarizability along the x axis is strongly affected, in particular for the larger molecules where this transition dominates the polarizability in x direction. Without this transition only a very small superlinearity persists (from 2.37 Å^3 to 2.98 Å^3 when going from NTCDA to PentTCDA). This shows that more than 90 % of the superlinearity results from the HOMO-LUMO transition of the molecules.

Due to the particular symmetry of the HOMO and LUMO wave functions, the polarizabilities in the y and z directions are not affected at all by the HOMO-LUMO transition. Apparently, this transition shuffles π electrons exclusively in the direction of the long axis of the molecule. In this context, it is interesting to note that in going from the HOMO to the LUMO, the number of nodal planes perpendicular to the long axis of the molecule increases from 5 to 6, with the consequence that the superposition of these two orbitals can shift charge along the long molecular axis effectively, as required for a polarization in this direction.

For an infinitely long molecule, i.e. a $(C_{10}H_4)_n$ polymer, electrons would form a metallic band and the static polarizability in x direction would diverge. Our five data points of Figure S9b constitute the onset of this divergence. For finite molecules, the band breaks up into confined states, which are the molecular orbitals[24], e.g. HOMO and LUMO. The longer the molecule, the more closely spaced are these confined states on the energy axis, i.e., the HOMO-LUMO gap reduces

from NTCDA to PentTCDA. According to Eq. S12 ($\chi \propto (E_n - E_m)^{-1}$), this leads to increasing contributions of corresponding electronic transitions to the low-frequency molecular polarizability. Note that the C_3 coefficients follow this trend, but they would not diverge at infinite molecular size.

It is well-known that the conjugation in aromatic systems can lead to a superlinear increase of the polarizability with molecular size, most prominently in elongated species such as oligomers[25–27]. The influence of this effect on the optical properties of molecules in solution is subject of intense research[28,29]. Here, we observe superlinearity for the first time directly in force experiments. One has to keep in mind that the superlinear rise of the dispersion interaction is smaller than the one in optical experiments, because the latter probe the polarizability at optical frequencies, while the dispersion potential is obtained by integration over imaginary frequencies up to $100\,\mathrm{eV}$.

S10 Full potential profile between PTCDA and Au(111)

Fig. 4b contains two separate interaction potentials for PTCDA with Au(111), one for the near-distance region, the other for the asymptotic region. Between them, they fully map out the potential profile.

The asymptotic potential is based on the data of this paper. In Fig. 4b we follow common practice and plot the potential for the flat molecule (molecular plane parallel to the surface). Since for a flat molecule all atoms in the molecule have identical z, we can sum over the C_3 coefficients

of all atoms in the molecule. The total potential thus becomes

$$V_{\text{flat mol-s}} = -M_{\text{eff}} \frac{C_3}{(z - z_0)^3}, \tag{S17}$$

with the effective number of carbon atoms M_{eff} (Eq. S4).

The orange potential profile is based on $C_3 = 70\,\text{kcal/mol}\text{Å}^3$ with $z_0 = 0\,\text{Å}$, as determined in Ref. 2 by fitting the range from 8 to 14.7Å and from 16.9 to 23.6Å in Fig. 2a (blue curve) with an expression based on the asymptotic potential Eq. S2. It is clear that applying this expression outside its range of validity, z_0 will decrease while C_3 will increase when approaching the surface, thus emulating the more shallow slope of the true potential for $z < 4.8\,\text{Å}$ and avoiding the singularity at z_0 (see Ref. 17 and Section S7 of the Supplementary Information). This behaviour can clearly be seen in Fig. 3b. We note here that although the $C_3 = 70\,\text{kcal/mol}\text{Å}^3$ and $z_0 = 0\,\text{Å}$ are 'unphysical' in the sense that they have been derived outside the asymptotic region, they do parameterize the true potential sufficiently well to yield a reasonable adsorption energy[2]. For clarity, the repulsive branch of the short-range potential (Ref. 2) has been omitted in Fig. 4b.

1. Toher, C. *et al.* Electrical transport through a mechanically gated molecular wire. *Phys. Rev. B* **83**, 155402 (2011).

2. Wagner, C., Fournier, N., Tautz, F. S. & Temirov, R. Measurement of the binding energies of the organic-metal perylene-teracarboxylic-dianhydride/Au(111) bonds by molecular manipulation using an atomic force microscope. *Phys. Rev. Lett.* **109**, 076102 (2012).

3. Bruch, L. W., Cole, M. W. & Zaremba, E. *Physical Adsorption Forces and Phenomena* (Dover Publications, Inc. Mineola, New York, 2007).

4. Zaremba, E. & Kohn, W. Van der Waals interaction between an atom and a solid surface. *Phys. Rev. B* **13**, 2270 (1976).

5. Ruiz, V. G., Liu, W., Zojer, E., Scheffler, M. & Tkatchenko, A. Density-functional theory with screened van der Waals interactions for the modeling of hybrid inorganic-organic systems. *Phys. Rev. Lett.* **108**, 146103 (2012).

6. Werner, W. S. M., Glantschnig, K. & Ambrosch-Draxl, C. Optical constants and inelastic electron-scattering data for 17 elemental metals. *J. Phys. Chem. Ref. Data* **38**, 1013 (2009).

7. Hirshfeld, F. L. Bonded-atom fragments for describing molecular charge densities. *Theor. Chim. Acta* **44**, 129 (1977).

8. Romaner, L., Nabok, D., Puschnig, P., Zojer, E. & Ambrosch-Draxl, C. Theoretical study of PTCDA adsorbed on the coinage metal surfaces, Ag(111), Au(111) and Cu(111). *New J. Phys.* **11**, 053010 (2009).

9. Tkatchenko, A. & Scheffler, M. Accurate molecular van der Waals interactions from ground-state electron density and free-atom reference data. *Phys. Rev. Lett.* **102**, 073005 (2009).

10. Lifshitz, E. M. The theory of molecular attractive forces between solids. *Soviet Phys. JETP* **2**, 73–83 (1956).

11. Tang, K. T. & Karplus, M. Padé-approximant calculation of the nonretarded van der Waals coefficients for two and three helium atoms. *Phys. Rev.* **171**, 70 (1968).

12. Johnson, E. R. & Becke, A. D. A post-Hartree-Fock model of intermolecular interactions. *J. Chem. Phys.* **123**, 024101 (2005).

13. Perdew, J., Burke, K. & Ernzerhof, M. Generalized gradient approximation made simple. *Phys. Rev. Lett.* **77**, 3865 (1996).

14. Blum, V. *et al.* Ab initio molecular simulations with numeric atom-centered orbitals. *Comput. Phys. Commun.* **180**, 2175 (2009).

15. Hauschild, A. *et al.* Molecular distortions and chemical bonding of a large π-conjugated molecule on a metal surface. *Phys. Rev. Lett.* **94**, 036106 (2005).

16. Rohlfing, M., Temirov, R. & Tautz, F. S. Adsorption structure and scanning tunneling data of a prototype organic-inorganic interface: PTCDA on Ag(111). *Phys. Rev B* **76**, 115421 (2007).

17. Rohlfing, M. & Bredow, T. Binding energy of adsorbates on a noble-metal surface: Exchange and correlation effects. *Phys. Rev. Lett.* **101**, 266106 (2008).

18. Monkhorst, H. J. & Pack, J. D. Special points for brillouin-zone integrations. *Phys. Rev. B* **13**, 5188 (1976).

19. Furche, F. Molecular tests of the random phase approximation to the exchange-correlation energy functional. *Phys. Rev B* **64**, 195120 (2001).

20. Marini, A., Garcia-Gonzalez, P. & Rubio, A. First-principles description of correlation effects in layered materials. *Phys. Rev. Lett.* **96**, 136404 (2006).

21. Harl, J. & Kresse, G. Cohesive energy curves for noble gas solids calculated by adiabatic connection fluctuation-dissipation theory. *Phys. Rev. B* **77**, 045136 (2008).

22. Lynch, D. & Hunter, W. *Handbook of Optical Constants of Solids*, 286 (Academic Press, Boston, 1985).

23. Rohlfing, M. Electronic excitations from a perturbative LDA+GdW approach. *Phys. Rev. B* **82**, 205127 (2010).

24. Koller, G. *et al.* Intra- and intermolecular band dispersion in an organic crystal. *Science* **317**, 351–355 (2007).

25. Zhao, M.-T., Singh, B. P. & Prasad, P. N. A systematic study of polarizability and microscopic third-order optical nonlinearity in thiophene oligomers. *J. Chem. Phys.* **89**, 5535–5541 (1988).

26. Thienpont, H., Rikken, G. L. J. A. & Meijer, E. W. Saturation of the hyperpolarizability of oligothiophenes. *Phys. Rev. Lett.* **65**, 2141 (1990).

27. Samuel, I. D. W. *et al.* Saturation of cubic optical nonlinearity in long-chain polyene oligomers. *Science* **265**, 1070 (1994).

28. Tretiak, S. & Mukamel, S. Density matrix analysis and simulation of electronic excitations in conjugated and aggregated molecules. *Chem. Rev.* **102**, 3171 (2002).

29. Kuzyk, M. G., Pérez-Moreno, J. & Shafei, S. Sum rules and scaling in nonlinear optics. *Phys. Rep.* **529**, 297 (2013).